Solid State Phenomena
ISSN: 1662-9779, Vol. 388, pp 127-140
doi:10.4028/p-NSOqa8

Submitted: 2026-01-19
Revised: 2026-02-16
Accepted: 2026-02-18
Online: 2026-04-15

Stochastic Forming Limit Curves: Construction of a Probabilistic Tool for Failure Assessment

Olivier AMELINE[a*] , Mohamed Yessine JEDIDI[b] , Augustin PERSOONS[c] , Carl LABERGERE[d]

Université de Technologie de Troyes, Unité de Recherche LASMIS

[a]olivier.ameline@utt.fr, [b]yessine.jedidi@utt.fr, [c]laugustin.persoons@utt.fr, [d]carl.labergere@utt.fr

Keywords: Forming Limit Curves, Stochastic Modeling, Experimental Variability

Abstract. The determination of Forming Limit Curves (FLCs) remains challenging due to their strong dependence on test conditions, material properties, and measurement methods. Significant variability is observed even for identical specimens, limiting the reliability of FLCs as deterministic tools. The goal of this work is to investigate non-deterministic FLC prediction in order to illustrate the impact of uncertainties and provide a basis for quantification of failure risks. The proposed approach uses the probabilistic framework where a model of input uncertainties including dependence is inferred from literature data using a Gaussian copula. A prediction model based on the linear perturbation technique is described and used to propagate input uncertainties using a Monte-Carlo approach. The obtained stochastic FLC is illustrated in terms of empirical confidence areas.

Introduction

Material failure in sheet metal forming is commonly assessed using a forming limit diagram (FLD), in which the maximal deformations observed during the process are plotted in the major–minor strain space and evaluated against the forming limit curve (FLC) [1]. The FLC delineates the boundary between stable and unstable deformation, representing the maximum strain the material can sustain before localized necking occurs. It serves as a critical threshold for safe forming operations, enabling the optimization of forming parameters and the reduction of defects and material waste.

FLCs have been used in metal forming industries for decades, motivating extensive research on their theoretical and experimental prediction. Analytical and numerical approaches commonly couple constitutive models with necking criteria under linear strain paths, as proposed by Swift [2], Hill [3], and Marciniak and Kuczyński [4]. More recent studies have extended the classical FLC framework toward a more comprehensive description of ductility limits for numerical forming simulations [5–7]. In parallel, several works describe the onset of necking within a homogeneous continuum framework using the linear perturbation technique, which avoids assuming an initial geometrical imperfection, in contrast to the Marciniak–Kuczyński approach [8–12]. Experimental investigations have been conducted to validate these numerical predictions [13–15].

Despite their widespread industrial use, forming limit curves (FLCs) have inherent limitations due to their strong sensitivity to testing conditions, material variability, and methodological choices in the identification of fracture and localized necking. Significant scatter in formability limits is commonly observed even for nominally identical specimens, showing that FLCs cannot be considered deterministic failure criteria.

The forming limit curve is then stochastic in nature and we propose a methodology to estimate its statistical properties, reflecting the distribution of strain states at localized necking. From an industrial perspective, the stochastic FLC provides a practical decision-making tool. By projecting the strain loading path experienced by a given part onto the stochastic FLC, manufacturers can evaluate the probability of failure associated with the forming operation. This probabilistic assessment enables a more reliable evaluation of formability and supports the optimization of forming process parameters, leading to improved robustness and reduced risk of defects.

This study follows a direct probabilistic approach: first, establishing a deterministic FLC model based on linear perturbation theory; second, characterizing uncertainties in the five model parameters through literature data; third, propagating these uncertainties via Monte Carlo simulation to generate stochastic FLC realizations. The computational efficiency of the underlying model enables direct Monte Carlo sampling without resorting to surrogate approximations. This provides manufacturers with confidence bounds reflecting both experimental and material variability, in order to support process control while reducing failure risks and overdesign. In practice, industrial users may then refine this prior uncertainty with available experimental data of their particular material using a Bayesian updating scheme.

The article is organized in three main sections. Section 1 presents the theoretical framework for forming limit prediction based on linear perturbation analysis. Section 2 describes parameter identification from literature data for CP-Ti. Section 3 details the probabilistic uncertainty modeling of these parameters, propagates the uncertainties through Monte Carlo simulation et analyzes the stochastic FLC properties.

Theoretical Model

The theoretical prediction of forming limit curves (FLCs) is done using the already well documented linear perturbation technique [8–12]. First, the equations of plasticity are solved analytically considering a uniform strain–stress state, which defines the homogeneous solution. Small perturbations are then superimposed onto this solution to assess the stability of the deformation and to predict the onset of strain localization.

Homogeneous solution.

The thin sheet is supposed to be incompressible and subjected to a plane stress state in the x-y laboratory system. Shear strains are neglected, the major strain is taken along the x direction and elasticity is ignored because large deformations are involved. A linear strain path is considered and characterized by the parameter ρ such that:

$$\rho = \varepsilon_{yy}/\varepsilon_{xx} = \text{const.} \tag{1}$$

The constitutive relation between stress and plastic strain rate components is defined using an associated flow rule (AFR), in which the equivalent stress σ_{Eq} is given by the Hill (1948) anisotropy criterion [16] and the hardening law σ_{Hard} is considered viscoplastic, such that:

$$\sigma_{Eq}(\boldsymbol{\sigma}) = \sqrt{F\sigma_{yy}^2 + G\sigma_{xx}^2 + H(\sigma_{xx} - \sigma_{yy})^2 + 2N\sigma_{xy}^2} \quad \text{and} \quad \sigma_{Hard}(\overline{\varepsilon}, \dot{\overline{\varepsilon}}) = \sigma_y(\overline{\varepsilon})\, \dot{\overline{\varepsilon}}^m, \tag{2}$$

where $\overline{\varepsilon}$ is the equivalent plastic strain, m is the strain-rate sensitivity, and the Hill coefficients F, G, H and N are expressed as functions of the Lankford parameters r_0, r_{45} and r_{90}:

$$F = \frac{r_0}{r_{90}(1+r_0)} \quad ; \quad G = \frac{1}{1+r_0} \quad ; \quad H = \frac{r_0}{1+r_0} \quad ; \quad N = \frac{1}{2}(F+G)(1+2\,r_{45})\,. \tag{3}$$

These assumptions are only approximate, as strain paths are typically neither shear-free nor linear in industrial processes. Nevertheless, they are reasonably satisfied in Nakazima and Marciniak tests, which are commonly employed in industry to construct experimental forming limit curves (FLCs). For HCP materials such as CP-Ti, the Hill (1948) yield criterion is also known to be less accurate than more advanced models that account for strong plastic anisotropy and tension–compression asymmetry [17, 18]. Despite these limitations, the present framework provides a practical starting point, as it can be implemented with a limited number of parameters and offers excellent computational efficiency. It can subsequently be applied to more complex models of anisotropy, and the resulting stochastic FLC can be further refined through Bayesian calibration based on experimental data.

Under quasi-static conditions, a uniform strain–stress state automatically satisfies the equilibrium and compatibility equations. The analytic resolution of the AFR and the condition of incompressibility lead to the homogeneous solution, expressed as a function of the major strain:

$$\sigma_{xx} = \frac{\dot{\varepsilon}_{xx}}{\dot{\overline{\varepsilon}}} \frac{F+H+H\rho}{FG+FH+GH} \sigma_y(\overline{\varepsilon}) \dot{\overline{\varepsilon}}^m \; ; \quad \sigma_{yy} = \frac{\dot{\varepsilon}_{xx}}{\dot{\overline{\varepsilon}}} \frac{H+(G+H)\rho}{FG+FH+GH} \sigma_y(\overline{\varepsilon}) \dot{\overline{\varepsilon}}^m \; ; \quad \sigma_{xy} = 0 \, ; \tag{4}$$

$$\frac{\dot{\overline{\varepsilon}}}{\dot{\varepsilon}_{xx}} = \frac{\overline{\varepsilon}}{\varepsilon_{xx}} = R(\rho) = \sqrt{\frac{F+G\rho^2+H(1+\rho)^2}{FG+FH+GH}} \; ; \quad \dot{\varepsilon}_{yy} = \rho \, \dot{\varepsilon}_{xx} \; ; \quad \dot{\varepsilon}_{zz} = -(1+\rho)\dot{\varepsilon}_{xx} \, . \tag{5}$$

Perturbation analysis. As illustrated in Fig. 1, a rotated coordinate system x_1-x_2 is defined to represent the orientation φ of a candidate localization band. Then, the homogeneous solution $\boldsymbol{P}(t) = \{\dot{\varepsilon}_{xx}, \dot{\varepsilon}_{yy}, \dot{\varepsilon}_{zz}, \dot{\varepsilon}_{xy}, \sigma_{xx}, \sigma_{yy}, \sigma_{xy}, \sigma_y, \overline{\varepsilon}\}^T$, defined in Eqs. (4)-(5), is perturbed in the direction x_1 such that:

$$\tilde{\boldsymbol{P}}(t,x,y) = \boldsymbol{P}(t) + \delta \boldsymbol{P} \exp[\eta t] \exp[i\xi(x\cos\varphi + y\sin\varphi)] \, , \tag{6}$$

where $\tilde{\boldsymbol{P}}$ is the perturbed solution, η is the growth rate, t is the time and ξ is the wave number.

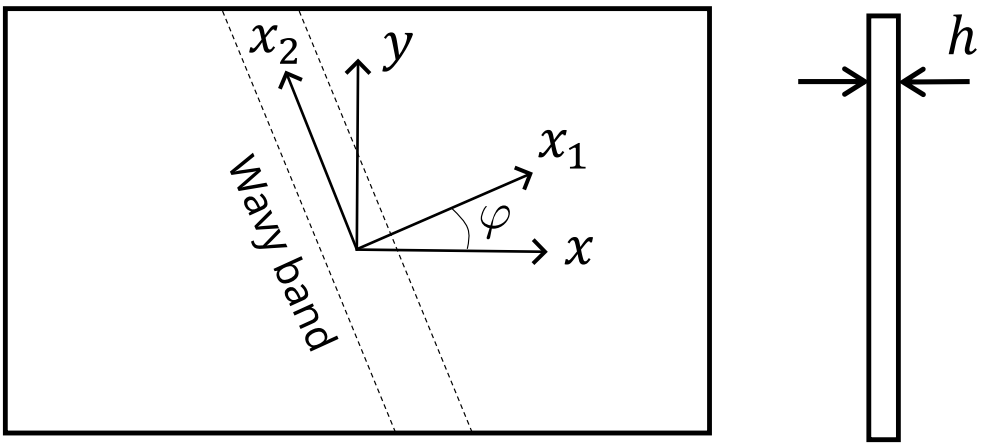

Fig. 1: Linear perturbation in thin sheet metal.

The perturbation $\tilde{\boldsymbol{P}}$ is introduced into the full set of plasticity equations, including the AFR, the equivalent stress, the hardening law, the equilibrium equations, the compatibility equation and the condition of incompressibility. By including the equilibrium equations, the perturbation is constrained to satisfy force balance between the inside and outside of the band. After linearization, the resulting system takes the form $\boldsymbol{M}\delta\boldsymbol{P} = \boldsymbol{0}$, with the onset of instability corresponding to the vanishing of the determinant of $\boldsymbol{M}$. This system provides conditions on the angle of the wavy band, φ, and the normalized growth rate, $\hat{\eta} = \eta/\overline{\varepsilon}$. By assuming that localized necking occurs along the direction of maximal rate of normalized growth rate, $d\hat{\eta}/d\overline{\varepsilon}$, Hu et al. [11] established that:

$$\varphi = \arctan\sqrt{-\rho} \quad \text{if} \quad \rho < 0 \quad ; \quad \varphi = 0 \quad \text{if} \quad \rho \geq 0. \tag{7}$$

With this additional condition, the normalized growth rate is expressed analytically as:

$$\hat{\eta} = \eta_1(\rho) \left[\eta_2(\rho) - \frac{\sigma_y'}{\sigma_y}(\overline{\varepsilon}) \right] , \tag{8}$$

where

$$\eta_1(\rho) = \frac{1}{m} \text{ if } \rho < 0 \quad ; \quad \eta_1(\rho) = \frac{(F+H+H\,\rho)^2}{(FG+FH+GH)\,\rho^2 + m\,(F+H+H\,\rho)^2} \text{ if } \rho \geq 0, \tag{9}$$

$$\eta_2(\rho) = \frac{\varepsilon_{xx}}{\overline{\varepsilon}}(1+\rho) \quad \text{if} \quad \rho < 0 \quad ; \quad \eta_2(\rho) = \frac{\varepsilon_{xx}}{\overline{\varepsilon}} \frac{F + G\rho^2 + H(1+\rho)^2}{F+H+H\rho} \quad \text{if} \quad \rho \geq 0. \tag{10}$$

These results are obtained by applying the formalism of Tóth et al. [9] or Hu et al. [11] to the more general hardening law of Eq. (2).

The perturbation becomes unstable when $\hat{\eta} > 0$, that is, for an equivalent plastic strain $\overline{\varepsilon}_i$ such that:

$$\frac{\sigma_y}{\sigma'_y}(\overline{\varepsilon}_i) = \frac{1}{\eta_2(\rho)}\,. \tag{11}$$

If the material is strain-rate insensitive, then $m \to 0$, which in practice can be considered by taking $m = 10^{-5}$ to avoid the singularity in the expression of $\eta_1(\rho)$ when $\rho < 0$. As a result, strain-rate insensitivity implies that the left part of the FLC is obtained by assigning localized necking to the equivalent strain $\overline{\varepsilon}_n = \overline{\varepsilon}_i$ where the normalized growth $\hat{\eta}$ diverges from $-\infty$ to $+\infty$. For the right part of the FLC ($\rho \geq 0$), the onset of necking is taken at the equivalent strain $\overline{\varepsilon}_n$ where the accumulated growth of the perturbation reaches a critical value E [11]:

$$\int_{\overline{\varepsilon}_i}^{\overline{\varepsilon}_n} \hat{\eta}\, d\overline{\varepsilon} = E. \tag{12}$$

For a strain-rate insensitive material, the critical value $\overline{\varepsilon}_n$ for localized necking thus verifies:

$$\overline{\varepsilon}_n = \overline{\varepsilon}_i \quad \text{if} \quad \rho < 0 \quad ; \quad \eta_1(\rho)\left[\eta_2(\rho)(\overline{\varepsilon}_n - \overline{\varepsilon}_i) - \ln\frac{\sigma_y(\overline{\varepsilon}_n)}{\sigma_y(\overline{\varepsilon}_i)}\right] = E \quad \text{if} \quad \rho \geq 0. \tag{13}$$

Once this critical value is known, the FLC is constructed in the ρ-$\overline{\varepsilon}$ space by plotting $\overline{\varepsilon}_n$ as a function of ρ. It can then be mapped into the ε_{xx}-ε_{yy} space using Eqs. (1) and (5).

Application to Experimental Data

In this section, the theoretical model is fitted to five experimental forming limit curves (FLCs) reported in literature [19–23].

Hardening law. The hardening law cannot be calibrated with either the published stress–strain curves or the models fitted to them, as tensile tests are generally limited to the onset of diffuse necking, whereas we need to model the material behavior beyond this stage. To address this difficulty, we use the $\rho < 0$ region of the experimental FLC to calibrate the hardening law. In the ε_{xx}-ε_{yy} space, this part of the curve is approximated by a decreasing straight line:

$$\text{when } \rho < 0, \quad \varepsilon_{xx} = -a\,\varepsilon_{yy} + b \quad \Leftrightarrow \quad \varepsilon_{xx} = b/(1+a\rho). \tag{14}$$

In this region, the equivalent plastic strain at necking takes the value $\overline{\varepsilon}_i$ defined by Eq. (11). The pair $(\overline{\varepsilon}, \sigma_y/\sigma'_y)$ corresponding to a point of the experimental FLC can thus be obtained as a function of ρ by computing the major strain ε_{xx} from Eq. (14), the equivalent plastic strain $\overline{\varepsilon}$ from Eq. (5), and the ratio σ_y/σ'_y from Eq. (11).

The resulting parametric curve is observed to be approximately linear for all studied FLCs, motivating the following hardening law:

$$\frac{\sigma_y}{\sigma'_y} = \alpha\,\bar{\varepsilon} + \beta, \quad \text{with} \quad \alpha = \frac{1/\eta_2(0) - 1/\eta_2(-0.5)}{b\,R(0) - 2b\,R(-0.5)/(2-a)} \quad ; \quad \beta = \frac{1}{\eta_2(0)} - \alpha\,b\,R(0). \tag{15}$$

This result is equivalent to choose a Swift hardening law, but with parameter values far different from usual because only the region posterior to diffuse necking is represented.

Model inference. From the foregoing, the construction of a theoretical FLC in the ρ-$\bar{\varepsilon}$ space with Eq. (13) requires five parameters: r_0, r_{90}, a, b and E. The Lankford r-values, r_0 and r_{90}, are directly available in the published literature (r_{45} is not involved due to the assumption of negligible shear strains). The coefficients a and b are readily obtained by linear regression of the left-hand side of the experimental FLC, while the threshold E is fitted to its right-hand side. The resulting parameter values are synthetized in Table 1. It should be noted that these data reflect not only the intrinsic variability of the material, but also the variability arising from testing conditions and measurement methods on FLC determination, since the parameters a, b and E are identified through an inverse approach by calibration against different experimental FLCs.

Table 1: Parameter values of the theoretical model that represents the published experimental data.

Article	r_0	r_{90}	a	b	E
Arrieux 1981	1.5	3	1.024	0.292	1.21
Chen 2005	4.2	2.1	1.209	0.340	0.71
Chamos 2013	1.5	3.75	0.993	0.302	1.58
Kim 2018	1.83	5.69	1.033	0.338	0.36
Wieckowski 2022	2.49	5.2	1.109	0.311	0.95

Fig. 2 presents the experimental data together with the theoretical model response, using the input parameters given in Table 1. A very good agreement is observed. However, the limited number of data points in the right-hand side of the experimental FLCs, together with the use of a hardening law calibrated on their left-hand side, tend to mask the model approximations. The assumptions adopted — particularly the Hill 1948 yield criterion — are generally not well suited to the industrial forming of CP-Ti. Even if the experimental data are well represented, these assumptions may affect the propagation of uncertainties within the model. Nevertheless, this simplified framework provides a practical basis for stochastic FLC prediction, which can later be refined employing more advanced models.

Uncertainty Modeling

On the previous section, the theoretical model has been successfully applied to represent experimental FLCs from literature. The goal of this section is to propose a first approach to estimate the statistical properties of the forming limit diagram of CP-TI considering the uncertainties related with the five input parameters (r_0, r_{90}, a, b and E) ang propagating them within the model.

The proposed approach uses a probabilistic framework [24], meaning the five inputs are considered as random variables and associated with probability distributions inferred from available data. The numerical model detailed in the previous sections allows us to obtain the forming limit diagram as a function of the five inputs. Since the input are stochastic in nature, the resulting forming limit diagram is a stochastic process. In other words, for any strain ratio ρ, the necking equivalent plastic strain $\bar{\varepsilon}$ is a random variable. The statistical properties of this stochastic FLC directly depends on the those of the five input parameters. It is then critical for the model of uncertainties assigned to the inputs to be representative of their actual variability.

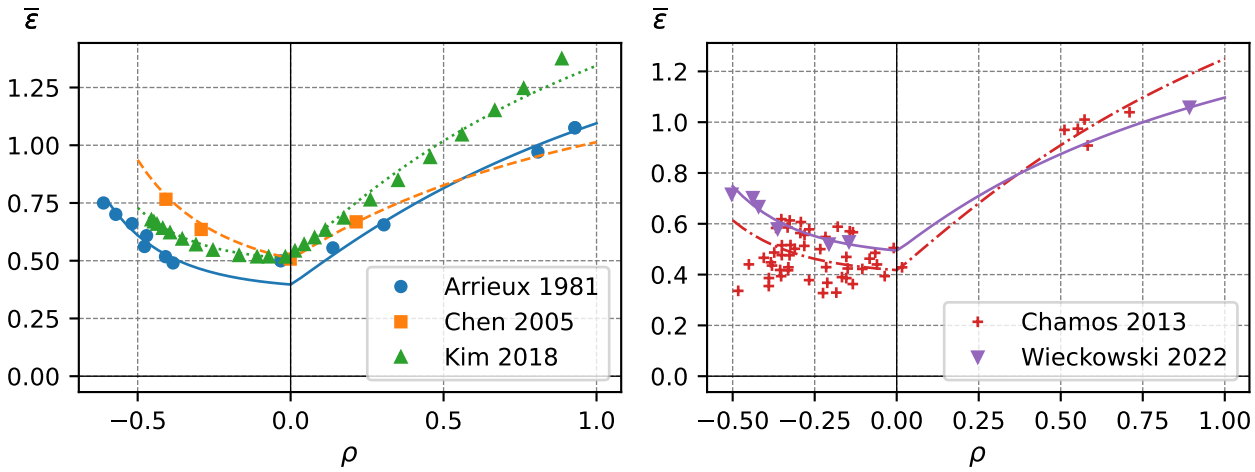

Fig. 2: Theoretical model fitted to experimental FLCs from litterature in ρ-$\bar{\varepsilon}$ space.

As previously mentioned, the model of uncertainty is inferred from a dataset collected from the literature (see Table 1). While only five instances of reports [19–23] including the necessary information to recover all five parameters are currently know to the authors, significantly more have been found reporting only the Lankford coefficients [25–41]. As a result, 25 instances of r_0 and r_{90} are used in the statistical study (see Table 2). Still, the small sample sizes present a significant challenge for statistical inference, requiring careful consideration of modeling assumptions.

Table 2: Values of r_0 and r_{90} used for marginal distribution inference [19–23, 25–41].

Ref.	r_0	r_{90}	Ref.	r_0	r_{90}	Ref.	r_0	r_{90}	Ref.	r_0	r_{90}	Ref.	r_0	r_{90}
[19]	1.50	3.00	[25]	2.30	4.72	[30]	1.19	3.13	[34]	1.55	3.88	[39]	0.74	1.68
[20]	1.50	3.75	[26]	0.95	2.85	[30]	1.46	3.36	[35]	1.70	4.89	[40]	2.11	3.62
[21]	4.20	2.10	[27]	2.20	4.89	[31]	1.51	5.17	[36]	2.34	4.86	[40]	2.66	5.23
[22]	1.83	5.69	[28]	2.29	4.70	[32]	1.58	6.80	[37]	1.71	2.67	[40]	1.46	2.66
[23]	2.49	5.20	[29]	3.84	5.45	[33]	2.11	4.85	[38]	2.46	5.65	[41]	1.22	3.55

Marginal distribution modeling. As a first step, each input parameter is associated with a marginal distribution function. The principle is to assume that the random variables follow a specific family of distributions, defined by shape or modal parameters that can be inferred from the data (e.g., a normal distribution parameterized by the mean and variance of the data).

The choice of a distribution family represents a strong assumption on the shape of the statistics and should be taken with caution, motivated by available knowledge about the parameter to be modeled and by as much statistical evidence as possible. Even so, it generally leads to imprecision when evaluating the statistics of extremely rare events (associated with the tails of the distributions). Nonparametric approaches [24] are generally to be preferred, but cannot be implemented in this context since they require a large amount of calibration data.

A first clue for choosing a distribution family is the domain on which the distribution is defined, i.e., whether there are bounds on the possible values of the parameter of interest. For instance, a normal distribution assumes all values in $\mathbb{R}$ are possible, which would not be suited to modeling a parameter taking only positive values. Other indicators could include information about statistical modes and the shape of the distribution (e.g., symmetry). Finally, one can resort to common practices in the literature for distributions of parameters of similar nature.

Since r_0, r_{90}, a, and b take only positive values, a lognormal distribution is arbitrarily selected among distributions with positive support. This choice is not uncommon in the literature [42, 43] and

involves assuming a multiplicative structure of the uncertainties, i.e., confidence intervals are defined as a nominal value multiplied and divided by a factor. The available data is currently too limited to clearly discriminate between possible distributions families, as also illustrated by the confidence intervals in the QQ-plots Fig. 3. While the lognormal family provides statistically satisfactory results, other choices could also be considered, such as the gamma or Weibull distributions. A formal evaluation of the sensitivity of the FLC statistics to this choice is planned, and the quantification of tail-related statistics is deemed outside the scope of the proposed approach.

The log-normal probability density function depends on two parameters, μ and s, corresponding respectively to the mean and standard deviation of the underlying normal distribution:

$$f_X(x) = \frac{1}{xs\sqrt{2\pi}} \exp\left(-\frac{(\ln x - \mu)^2}{2s^2}\right) \tag{16}$$

The parameters of the four log-normal distributions were then obtained using maximum likelihood estimation over the available data. The resulting values are reported in Table 3.

The parameter E takes only positive values, no skewness is observable in the data (see Fig. 3), and no common practice appears in the literature. A uniform distribution was adopted as a maximum-entropy representation given only the observed range $[E_{\text{min}}, E_{\text{max}}]$ [24]. This approach imposes strict bounds on the values of E and is therefore conservative (it assumes no values more extreme than those observed will occur). It is, however, a minimal-assumption approach in such a case of limited information, as it avoids unsupported distributional assumptions.

The quality of the calibration is illustrated in Fig. 3, where on the left-hand side the histograms of calibration data are drawn together with the fitted distributions. The figures qualitatively illustrate the agreement in the shape of the fitted and empirical distributions for r_0 and r_{90}. For the other three parameters, the low amount of available data makes it too difficult to draw conclusions from histograms.

The right-hand side of the figure shows quantile–quantile plots of empirical data as a function of the fitted quantiles. These standard graphs show the correspondence between statistical quantiles of the calibration data and the fitted model, and can be interpreted analogously to the calibration plots used in regression modeling, showing the predicted value as a function of the true one. In addition the 95% confidence intervals associated with each empirical quantiles are drawn, based on an asymptotic normal assumption (considering each data point is independent and identically distributed). In these figures, the fit appears clearly to be in acceptable accordance with the data, especially for central values (i.e., non-extreme ones).

Table 3: Probabilistic models for material parameters.

Parameter	Distribution	Parameter 1	Parameter 2
r_0	Lognormal	$\mu_{r_0} = 5.65 \times 10^{-1}$	$\sigma_{r_0} = 3.77 \times 10^{-1}$
r_{90}	Lognormal	$\mu_{r_{90}} = 1.333$	$\sigma_{r_{90}} = 3.36 \times 10^{-1}$
a	Lognormal	$\mu_a = 6.84 \times 10^{-2}$	$\sigma_a = 7.04 \times 10^{-2}$
b	Lognormal	$\mu_b = -1.15$	$\sigma_b = 6.10 \times 10^{-2}$
E	Uniform	$E_{\text{min}} = 7.11 \times 10^{-1}$	$E_{\text{max}} = 1.58$

Dependence structure modeling. The five input parameters are physically interdependent: processing history is bound to affect anisotropy (r_0, r_{90}), hardening response (a, b), and necking threshold E. This physical intuition stresses the fact that, while random, the five inputs are likely correlated. Ignoring these dependencies would degrade the relevance of the FLC statistical properties.

Many ways exist in the literature to model the dependence between random variables. The simplest is to use a linear correlation matrix (e.g., in a multivariate Gaussian distribution). However, a correlation matrix cannot be used directly in our case since the five marginals are not Gaussian. A standard and efficient way of using the correlation matrix in such a case is a Gaussian copula [24].

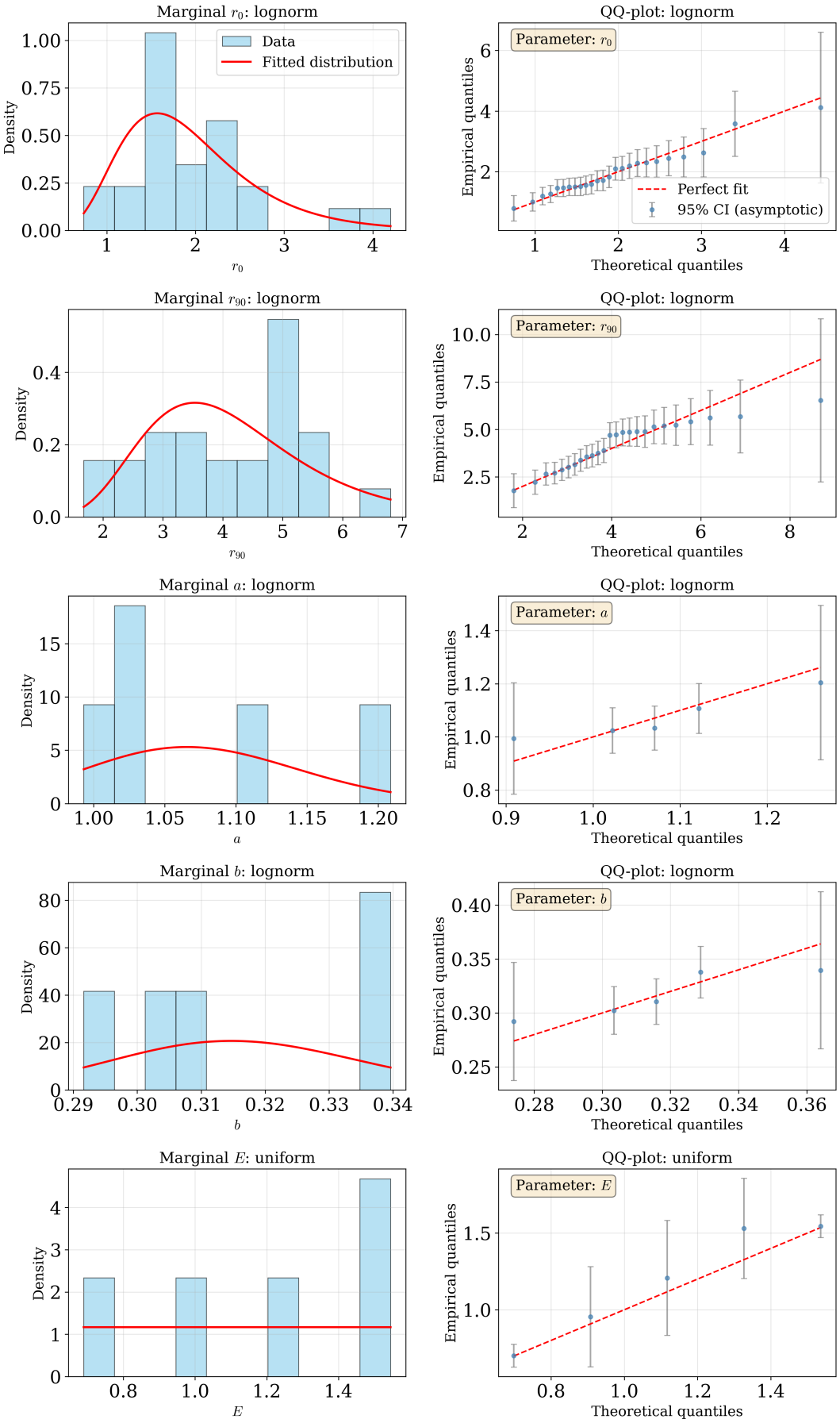

Fig. 3: Illustration of the inference of the five marginal distributions, including (left) histograms of available data and fitted distributions and (right) empirical quantiles of data vs. quantiles of the fitted distributions.

The principle is to apply a transform to the input parameters in order to define five random variables that are normally distributed. This transform is called the probability integral transform and relies on the fact that, for any random variable X following a distribution f with cumulative distribution function (CDF) F, $F(X)$ is a random variable following a uniform distribution. Using the inverse transform, one can also state that if U follows a uniform distribution and Φ^{-1} is the inverse of the standard Gaussian CDF, then $\Phi^{-1}(U)$ follows a Gaussian distribution. It follows that, for any random variable X, $\Phi^{-1}(F(X))$ follows a standard Gaussian distribution. The principle behind the Gaussian copula is to model the transformed, normally distributed random variables as a simple multivariate Gaussian characterized by a correlation matrix inferred from the transformed calibration data.

Calibrating a Gaussian copula in this case simply means applying the probability integral transform to the calibration data (using the CDFs of the marginals). The covariance matrix **R** of the transformed data is then estimated via maximum likelihood. Generating Monte Carlo samples of the five inputs respecting the dependence structure simply means generating samples of the multivariate Gaussian with covariance **R** and applying the inverse transform to those samples.

In order to evaluate the relevance of the calibrated copula, Monte Carlo samples are generated and scatterplots are drawn showing the trends between pairwise variables. On top of these simulated data points, the actual calibration data are drawn to illustrate the fit qualitatively. These plots are presented in the lower-triangular panels of Fig. 4, where each row and column represent one of the five inputs. The figure illustrates a satisfactory fit, even though the limited data make it hard to draw quantitative conclusions on the goodness of fit.

In addition, the diagonal panels of Fig. 4 represent the histograms of simulated marginal data together with the histogram of each individual calibration dataset. This information is related to the goodness of fit of the marginals, already illustrated in Fig. 3.

Finally, the upper triangle of the figure represents the correlation coefficients between the pairs of inputs, showing a quantitative measure of the correlations. These values are indicative of the strength of the correlation between pairs of variables but should be treated as indicative only, since they assume a linear correlation that does not strictly hold outside the space of the transformed (normally distributed) random variables.

It is, however, worth noting that the choice of a Gaussian copula imposes strong limitations with $n = 5$. The validation of **R** is impossible with such limited data, meaning it is not possible to evaluate the relevance of the fitted copula with respect to epistemic uncertainties. It is therefore important to stress the statistical limitations of this approach: with such limited calibration data, only broad statistical tendencies and sensitivities should be studied. In particular, any results related to rare events and the tails of distributions should not be interpreted quantitatively.

Uncertainty propagation. As previously mentioned, since the input parameters of the model are random variables, the output FLC is effectively a stochastic process, meaning that for each value of ρ, the equivalent necking plastic strain $\bar{\varepsilon}$ is a random variable. However, direct propagation of the random variables through the model is not trivial, and the analytical expression or closed-form properties of this stochastic process are not available. In order to obtain a numerical estimation of these properties, a Monte Carlo approach was implemented.

Using the model of uncertainty calibrated as described in the previous two sections, $N = 10{,}000$ random samples of the five input parameters were generated (Monte Carlo simulations). For each sample, the corresponding forming limit diagram is recovered using the numerical model described in the first two sections, resulting in a population of N randomly generated FLCs. For the sake of convenience, FLCs are expressed in the space of equivalent plastic strain $\bar{\varepsilon}$ vs. strain ratio ρ instead of the usual major strain vs. minor strain. Both spaces are equivalent, but the latter imposes a repartition of curve data following a polar basis, which is less straightforward to analyze.

This Monte Carlo population of FLCs provides, for each evaluated value of ρ, a population of N values of $\bar{\varepsilon}$. Using this population, empirical confidence intervals (CIs) were estimated, allowing us to illustrate the variability of the stochastic FLC, as presented in Fig. 5. In other words, for each value

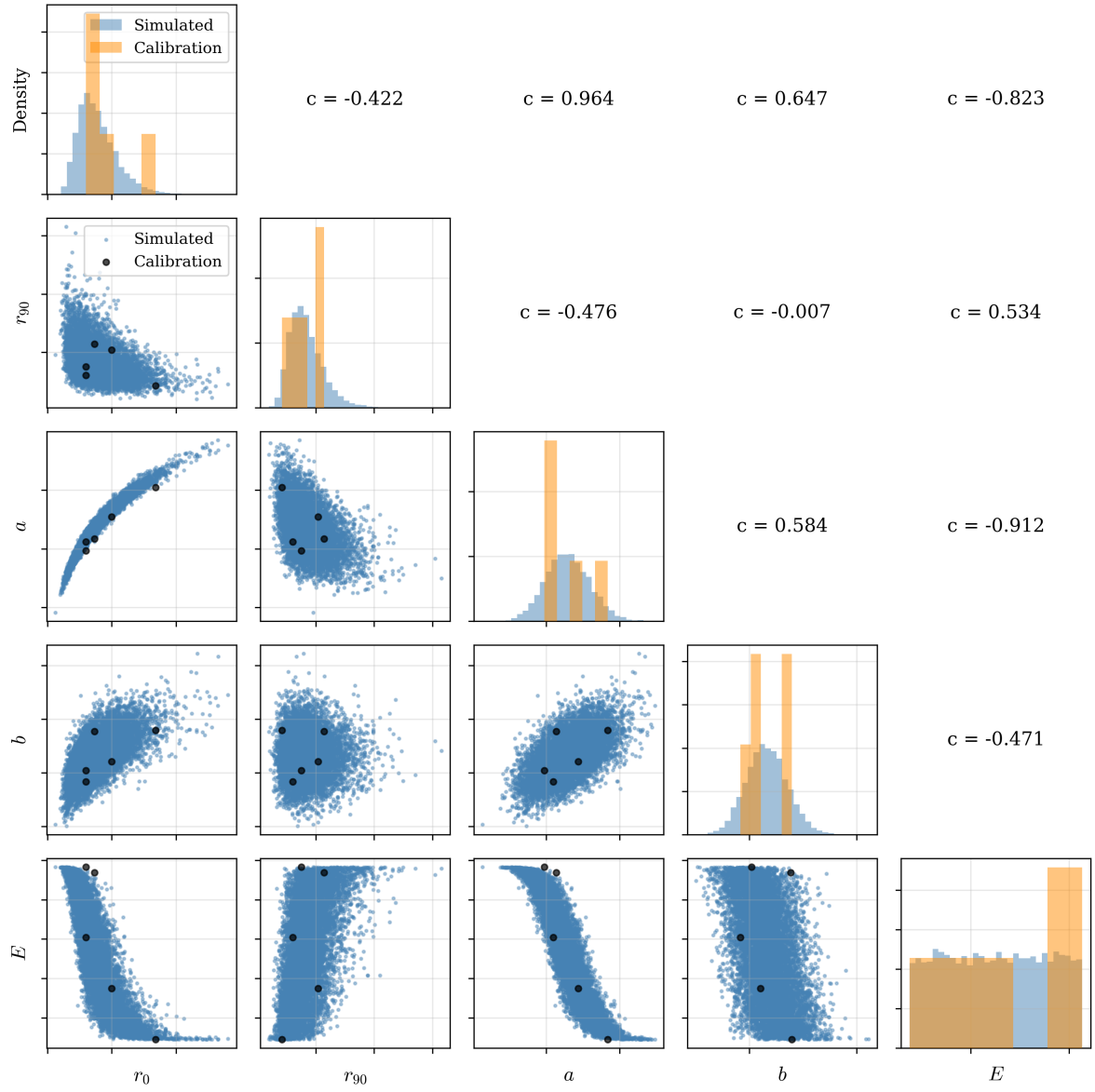

Fig. 4: Illustration of the dependence between input variables and the fitted copula with: (diagonal) histograms of marginal data and simulated samples; (upper triangle) correlation values between pairwise variables; (lower triangle) pairwise input scatterplots of calibration data and samples simulated using the fitted copula.

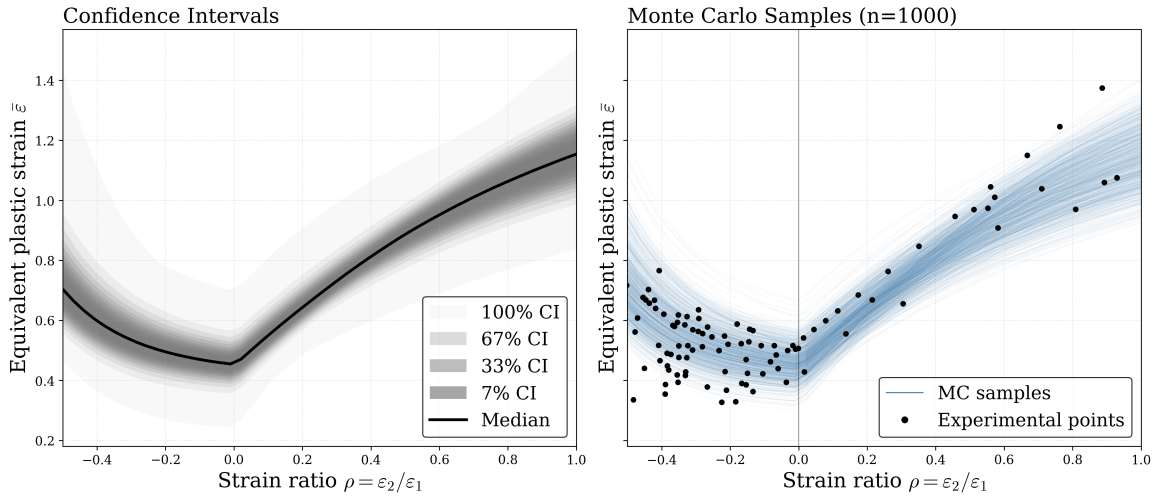

Fig. 5: Stochastic FLCs: (left) median (solid line) and confidence intervals (shaded regions) from 10,000 Monte Carlo realizations; (right) illustration of 1,000 Monte Carlo samples of FLCs.

of ρ, the value of the critical equivalent plastic strain can be empirically associated with confidence intervals, i.e., $\bar{\varepsilon}$ has a probability p% of being in the interval $[\underline{CI}_p, \overline{CI}_p]$. In the figure, increasingly larger confidence intervals are shown with increasingly lighter gray areas, showing the evolution of the stochasticity of the FLC for all values of ρ.

From a methodological point of view, it can be observed that the uncertainties related to the forming limit threshold are higher at the boundary values of ρ and respectively narrower around $\rho = 0$. The figure also illustrates the fact that the variance of $\bar{\varepsilon}$ is not a trivial function (e.g., constant) of ρ, but follows a more complex trend with competing tendencies. These results suggest investigating another property of the stochastic FLC, namely the sensitivity of $\bar{\varepsilon}$ to each input parameter.

In a practical context, obtaining the statistics of the FLC as presented in Fig. 5 means an engineer can draw statistical conclusions regarding the safety of a given forming process. The principle would be to gather, from mechanical simulations, the critical deformation paths of the process. For each path, it is then possible to obtain an *a priori* probability of fracture of the material. Such information should then be analyzed with respect to the quality targets for the process and help in making well-informed design and manufacturing decisions. This approach provides more nuanced and richer information than a simple deterministic curve, accounting for the observed uncertainties related to the quantity of interest. Moreover, this ”a priori” uncertainty quantification can be complemented with extra data if available. Such that an industrial user could use a Bayesian updating scheme to refine the uncertainty prediction to better represent the variability of its actual material properties.

Future work directions. The next goals in this study are first to propose a stochastic model for the FLC, going beyond empirical Monte Carlo (MC) estimations of its statistical properties. The second objective is to link the stochastic FLC with a forming simulation and propose a framework for uncertainty propagation to engineering decisions, as well as an active learning scheme [44] to reduce the FLC uncertainties with a semi-optimal experimental campaign.

A first approach would be to use a Gaussian process regression (GPR) model to emulate the stochastic FLC, but such an approach includes specific challenges:

(1) The covariance structure of the FLC needs to be thoroughly studied. It exhibits non-stationary variance that peaks at extreme ρ values and reaches a local minimum near plane strain. Future investigations entail evaluating the empirical variogram across ρ to detect non-stationarity, functional principal component analysis of Monte Carlo ensembles to identify dominant variation modes, and spectral density estimation of de-trended trajectories to determine correlation length scales.

(2) The physics requires FLCs to be decreasing for $\rho < 0$ and increasing for $\rho > 0$. Standard GP kernels violate these constraints. Constrained GP formulations (e.g., monotonic warping or projection onto shape-preserving reproducing kernel Hilbert spaces) require investigation.

(3) Since FLC realizations derive from only five random variables, the output process is inherently low-rank. Standard GP assumptions of infinite-dimensional latent functions may be over-parameterized.

An alternative approach would consist of calibrating a surrogate on the 6D space $(\rho, r_0, r_{90}, a, b, E)$, thus respecting the deterministic structure and avoiding process-level constraints.

Conclusion

This study has established a probabilistic framework for forming limit curve prediction in commercially pure titanium, addressing the inherent uncertainty that limits traditional deterministic approaches. By combining a computationally efficient linear perturbation model with literature-based parameter characterization and Monte Carlo propagation, the probabilistic approach can propagate material property uncertainties into quantifiable dispersion in FLC predictions. The computational efficiency of the underlying model—requiring only simple numerical integration—enabled direct Monte Carlo sampling without surrogate approximations.

Future efforts will focus on experimental validation through Nakazima testing with full-field DIC measurement to confirm predicted confidence intervals. Methodological extensions include hierarchical Bayesian calibration to distinguish uncertainty types, and investigation of constrained Gaussian process formulations to model the FLC directly as a stochastic process while respecting physics-based monotonicity requirements. The low-dimensional nature of the underlying parameter space suggests that direct surrogate modeling in $(\rho, r_0, r_{90}, a, b, E)$ may prove more tractable than standard process-level GP emulation.

This work aims to provide manufacturers with an updatable, uncertainty-aware design tool that balances risk reduction against overdesign, directly addressing industrial needs for robust sheet forming process control. This probabilistic framework provides the first quantitative uncertainty assessment for CP-Ti forming limits based on literature data. While the small sample size necessitates strong assumptions, the methodology is parsimonious, computationally efficient, and explicitly acknowledges its limitations. The resulting confidence intervals should be interpreted as *plausible bounds* rather than precise frequency-based probabilities. The modular structure facilitates continuous refinement as new data and theoretical advances emerge, moving toward true predictive uncertainty quantification for sheet metal forming applications.

*

References

[1] S. P. Keeler, Plastic Instability and Fracture in Sheets Stretched over Rigid Punches, Massachusetts Institute of Technology (1961).

[2] H. Swift, Plastic Instability under Plane Stress, *J. Mech. Phys. Solids*. 1 (Oct. 1952) 1–18.

[3] R. Hill, On Discontinuous Plastic States, with Special Reference to Localized Necking in Thin Sheets, *J. Mech. Phys. Solids*. 1 (Oct. 1, 1952) 19–30.

[4] Z. Marciniak, K. Kuczyński, Limit Strains in the Processes of Stretch-Forming Sheet Metal, *Int J Mech Sci*. 9 (Sept. 1967) 609–620.

[5] L. I. Besong, J. Buhl, M. Bambach, Increasing Formability in Hole-Flanging through the Use of Punch Rotation Based on Temperature and Strain Rate Dependent Forming Limit Curves, *Int J Mater Form*. 15 (May 2022) 37.

[6] C. Suntaxi, J. López-Fernández, G. Centeno, C. Vallellano, Novel Test Designs for Assessing the Shear Fracture Forming Limit in Thin-Walled Tubes, *Thin-Walled Struct.* 210 (May 2025) 113048.

[7] G. Mainguy, T. Balan, X. Lemoine, Comparison of Nonlinear Strain Path Correction Models for the FLD Characterization, *MATEC Web Conf.* 408 (2025) 01064.

[8] D. Dudzinski, A. Molinari, Perturbation Analysis of Thermoviscoplastic Instabilities in Biaxial Loading, *Int. J. Solids Struct.* 27 (1991) 601–628.
[9] L. Tóth, D. Dudzinski, A. Molinari, Forming Limit Predictions with the Perturbation Method Using Stress Potential Functions of Polycrystal Viscoplasticity, *Int J Mech Sci*. 38 (1996) 805–824.
[10] N. Boudeau, A. Lejeune, J. Gelin, Influence of Material and Process Parameters on the Development of Necking and Bursting in Flange and Tube Hydroforming, *J. Mater. Process. Technol.* 125–126 (Sept. 2002) 849–855.
[11] Q. Hu, L. Zhang, Q. Ouyang, X. Li, X. Zhu, J. Chen, Prediction of Forming Limits for Anisotropic Materials with Nonlinear Strain Paths by an Instability Approach, *Int J Plast*. 103 (2018) 143–167.
[12] M. Jedidi, M. Ben Bettaieb, F. Abed-Meraim, M. Khabou, A. Bouguecha, M. Haddar, Prediction of Necking in HCP Sheet Metals Using a Two-Surface Plasticity Model, *Int J Plast*. 128 (May 2020) 102641.
[13] S. Msolli, H. Badreddine, C. Labergere, M. Martiny, G. Robin, M. Jrad, K. Saanouni, F. Choquart, Experimental Characterization and Numerical Prediction of Ductile Damage in Forming of AA1050-O Sheets, *Int J Mech Sci*. 99 (Aug. 2015) 262–273.
[14] M. Y. Jedidi, V. Valle, Experimental Investigation to Determine Necking of Commercially Pure Titanium Sheets Using a Time-of-Flight Camera and Heaviside-digital Image Correlation, *Opt. Lasers Eng.* 164 (May 2023) 107529.
[15] B. Sarema, S. Matope, M. Nagel, A. Sterzing, Material Characterisation Experiments and Data Preparation for a Finite Element Analysis of the Deep Drawing Process Using AA 1050-O, *J. Manuf. Mater. Process.* 9 (Jan. 24, 2025) 33.
[16] R. Hill, A Theory of the Yielding and Plastic Flow of Anisotropic Metals, *Proc. R. Soc. Lond. Ser. A*. 193 (May 27, 1948) 281–297.
[17] O. Cazacu, B. Plunkett, F. Barlat, Orthotropic Yield Criterion for Hexagonal Closed Packed Metals, *Int J Plast*. 22 (July 1, 2006) 1171–1194.
[18] S.-H. Wu, N.-N. Song, F. M. Andrade Pires, A. D. Santos, Prediction of Forming Limit Diagrams for Materials with HCP Structure, *Acta Metall. Sin. (Engl. Lett.)* 28 (Dec. 2015) 1442–1451.
[19] R. Arrieux, C. Bedrin, F. Le Maître, Determination of Forming Limit Diagrams for Titanium Sheets, *CIRP Ann Manuf Technol*. 30 (1981) 189–192.
[20] A. N. Chamos, G. N. Labeas, D. Setsika, Tensile Behavior and Formability Evaluation of Titanium-40 Material Based on the Forming Limit Diagram Approach, *J Mater Eng Perform*. 22 (2013) 2253–2260.
[21] F.-K. Chen, K.-H. Chiu, Stamping Formability of Pure Titanium Sheets, *J Mater Process Technol*. 170 (2005) 181–186.
[22] Y.-S. Kim, B.-H. Lee, S.-H. Yang, Prediction of Forming Limit Curve for Pure Titanium Sheet, *Trans Nonferrous Met Soc China*. 28 (2018) 319–327.
[23] W. Więckowski, M. Motyka, J. Adamus, P. Lacki, M. Dyner, Numerical and Experimental Analysis of Titanium Sheet Forming for Medical Instrument Parts, *Mater.* 15 (2022).
[24] C. Soize, Uncertainty Quantification: An Accelerated Course with Advanced Applications in Computational Engineering, Springer International Publishing, Cham, 2017.
[25] J. Adamus, Theoretical and Experimental Analysis of the Sheet-Titanium Forming Process, *Arch. Metall. Mater.* 54 (2009) 705–709.
[26] M. Baral, T. Hama, E. Knudsen, Y. P. Korkolis, Plastic Deformation of Commercially-Pure Titanium: Experiments and Modeling, *Int J Plast*. 105 (2018) 164–194.
[27] N. Benmhenni, S. Bouvier, R. Brenner, T. Chauveau, B. Bacroix, Micromechanical Modelling of Monotonic Loading of CP α-Ti: Correlation between Macroscopic and Microscopic Behaviour, *Mater. Sci. Eng. A*. 573 (2013) 222–233.

[28] D. Ceccaldi, T. Baudin, R. Penelle, On Critical Polyhedrons for B.C.C. and H.C.P. Materials, *Int J Plast*. 15 (1999) 209–222.
[29] T. M. Chinapareddygari, C. Ravishankar, K. Thangaraj, S. K. Albert, U. Borah, A. K. Vesangi, R. K. Gupta, Stretchability of Commercial Purity Titanium Sheet, *Metall Mat Trans A Phys Metall Mat Sci*. 50 (2019) 5602–5613.
[30] X. Huang, K. Suzuki, Y. Chino, Improvement of Stretch Formability of Pure Titanium Sheet by Differential Speed Rolling, *Scripta Mater*. 63 (2010) 473–476.
[31] J. Kim, Q. T. Pham, J. Ha, Y. S. Kim, Constitutive Modeling of Commercial Pure Titanium Sheet Based on Non-Associated Flow Rule and Differential Hardening, *Int J Mech Sci*. 230 (2022).
[32] K. J. Kim, C. Kim, K. M. Min, J. Kim, H. J. Bong, Experimental Determination of Forming Limit Diagram of an Ultra-thin Pure Titanium Sheet, *Trans. Mater. Process.* 33 (2024) 465–471.
[33] A. Le Port, F. Toussaint, R. Arrieux, Finite Element Study and Sensitive Analysis of the Deep-Drawing Formability of Commercially Pure Titanium, *Int. J. Mater. Form.* 2 (2009) 121–129.
[34] C. Nagano, T. Kuwabara, Y. Shimada, R. Kawamura, Measurement of Differential Hardening under Biaxial Stress of Pure Titanium Sheet, *IOP Conf. Ser. Mater. Sci. Eng.* 418 (2018).
[35] Q. T. Pham, M. G. Lee, Y. S. Kim, Characterization of the Isotropic-Distortional Hardening Model and Its Application to Commercially Pure Titanium Sheets, *Int J Mech Sci*. 160 (2019) 90–102.
[36] B. Revil-Baudard, O. Cazacu, E. Massoni, Room-Temperature Plastic Behavior and Formability of a Commercially Pure Titanium: Mechanical Characterization, Modeling, and Validation, *Int. J. Solids Struct.* 228 (2021).
[37] A. Singh, S. Basak, L. P. P.S., G. G. Roy, M. N. Jha, M. Mascarenhas, S. K. Panda, Prediction of Earing Defect and Deep Drawing Behavior of Commercially Pure Titanium Sheets Using CPB06 Anisotropy Yield Theory, *J. Manuf. Processes*. 33 (2018) 256–267.
[38] L. Tabourot, P. Balland, J. Raujol-Veille, M. Vautrot, C. Depres, F. Toussaint, Compartmentalized Model for the Mechanical Behavior of Titanium, *Key Eng Mat*. 504–506 (2012) 673–678.
[39] M. Tournay, J.-S. Lecomte, C. Schuman, Y. Zhang, □. Fleury, Achieving Basal Texture in Pure Titanium: Process Implementation and Mechanical Property Evaluation, *Mater Charact*. 223 (2025).
[40] L. Wang, H. Zhang, G. Huang, M. Cao, X. Cao, E. Mostaed, M. Vedani, Formability and Anisotropy of the Mechanical Properties in Commercially Pure Titanium after Various Routes Normal and Different Speed Rolling, *J Mater Res*. 31 (2016) 3372–3380.
[41] J. W. Won, C. H. Park, J. Hong, C. S. Lee, S.-G. Hong, Simultaneous Improvement in the Strength and Formability of Commercially Pure Titanium via Twinning-induced Crystallographic Texture Control, *Sci. Rep.* 9 (2019).
[42] Z. Bazaras, V. Lukoševičius, A. Vilkauskas, R. Česnavičius, Probability Assessment of the Mechanical and Low-Cycle Properties of Structural Steels and Aluminium, *Metals*. 11 (June 4, 2021) 918.
[43] K. Prasad, D. Kumar, H. Krishnaswamy, D. K. Banerjee, Uncertainties in the Swift Hardening Law Parameters and Their Influence on the Flow Stress and the Hole Expansion Behavior of Dual-Phase (DP600) Steel Specimens, *J. of Materi Eng and Perform*. 32 (Oct. 2023) 9206–9220.
[44] A. Persoons, P. Wei, M. Broggi, M. Beer, A New Reliability Method Combining Adaptive Kriging and Active Variance Reduction Using Multiple Importance Sampling, *Struct Multidisc Optim*. 66 (June 2023) 144.